PHYSICAL REVIEW D **93,** 113015 (2016)

Deuterium target data for precision neutrino-nucleus cross sections

Aaron S. Meyer[*]
Enrico Fermi Institute and Department of Physics, The University of Chicago, Chicago, Illinois 60637, USA and Fermi National Accelerator Laboratory, Batavia, Illinois 60510, USA

Minerba Betancourt[†]
Fermi National Accelerator Laboratory, Batavia, Illinois 60510, USA

Richard Gran[‡]
Department of Physics and Astronomy, University of Minnesota—Duluth, Duluth, Minnesota 55812, USA

Richard J. Hill[§]
TRIUMF, 4004 Wesbrook Mall, Vancouver, British Columbia, V6T 2A3 Canada, Perimeter Institute for Theoretical Physics, Waterloo, Ontario, N2L 2Y5 Canada, Enrico Fermi Institute and Department of Physics, The University of Chicago, Chicago, Illinois 60637, USA

(Received 20 March 2016; published 23 June 2016)

Amplitudes derived from scattering data on elementary targets are basic inputs to neutrino-nucleus cross section predictions. A prominent example is the isovector axial nucleon form factor, $F_A(q^2)$, which controls charged current signal processes at accelerator-based neutrino oscillation experiments. Previous extractions of F_A from neutrino-deuteron scattering data rely on a dipole shape assumption that introduces an unquantified error. A new analysis of world data for neutrino-deuteron scattering is performed using a model-independent, and systematically improvable, representation of F_A. A complete error budget for the nucleon isovector axial radius leads to $r_A^2 = 0.46(22)\ \mathrm{fm}^2$, with a much larger uncertainty than determined in the original analyses. The quasielastic neutrino-neutron cross section is determined as $\sigma(\nu_\mu n \to \mu^- p)|_{E_\nu = 1\ \mathrm{GeV}} = 10.1(0.9) \times 10^{-39}\ \mathrm{cm}^2$. The propagation of nucleon-level constraints and uncertainties to nuclear cross sections is illustrated using MINERvA data and the GENIE event generator. These techniques can be readily extended to other amplitudes and processes.

DOI: 10.1103/PhysRevD.93.113015

I. INTRODUCTION

Current and next generation accelerator-based neutrino experiments are poised to answer fundamental questions about neutrinos [1–5]. Precise neutrino scattering cross sections on target nuclei are critical to the success of these experiments. These cross sections are computed using nucleon-level amplitudes combined with nuclear models. Determination of the requisite nuclear corrections presently relies on data-driven modeling [6–9] employing experimental constraints [10–17]. *Ab initio* nuclear computations are beginning to provide additional insight [18–20]. Regardless of whether nuclear corrections are constrained experimentally or derived from first principles, independent knowledge of the elementary nucleon-level amplitudes is essential. In this paper, we address the problem of model-independent extraction of elementary amplitudes from scattering data, and the propagation of rigorous uncertainties through to nuclear observables.

The axial-vector nucleon form factor, $F_A(q^2)$, is a prominent source of uncertainty in any neutrino cross section program. While the techniques employed in the present paper may be similarly applied to other elementary amplitudes, such as vector form factors [21], we focus on the axial-vector form factor, which is not probed directly in electron scattering measurements, and which has large uncertainty.

The axial form factor is constrained, with a varying degree of model dependence, by neutron beta decay [22], neutrino scattering on nuclear targets heavier than deuterium [11,23–28], pion electroproduction [29] and muon capture [30]. Existing data for the neutrino-deuteron scattering process provide the most direct access to the shape of the axial-vector nucleon form factor. The assumption of a neutron at rest and barely bound in the laboratory frame permits unambiguous energy reconstruction, eliminating flux uncertainties. The abundant neutrino scattering data on heavier targets involve degenerate uncertainties from neutrino flux, and from large and model-dependent nuclear corrections, complicating the extraction of nucleon-level amplitudes. Antineutrino scattering on hydrogen would entirely eliminate even the nuclear corrections required for deuterium, but there are no high-statistics data for this process. Given the

---

[*] asmeyer2012@uchicago.edu
[†] betan009@fnal.gov
[‡] rgran@d.umn.edu
[§] richardhill@uchicago.edu

importance of deuterium data for the axial form factor, it is imperative to quantify the constraints from existing data.

In this paper, we present the charged-current axial-vector nucleon form factor and error budget determined from neutrino-deuterium scattering data. In place of the dipole assumption [cf. Eq. (9) below] used in previous analyses of the form factor, we employ the model-independent z expansion[1] parametrization. The resulting uncertainty is significantly larger than found in previous analyses [29,54,55] of the deuterium constraint on the axial form factor using multiple data sets. This larger uncertainty results from removing the dipole assumption, and from including systematic errors for experimental acceptance corrections and for model-dependent deuteron corrections. The new constraints may be readily implemented in nuclear models and neutrino event generators.

The remainder of the paper is structured as follows. In Sec. II we introduce the deuterium data sets and perform fits to the dipole model for the axial form factor. This is done in order to compare with original publications, and to isolate the impact of form factor shape assumptions versus other inputs or data selections. In Sec. III we review the relevant z expansion formalism, and redo fits from Sec. II replacing dipole with z expansion. Several features of these fits indicate potentially underestimated systematic errors in corrections that were applied to data in the original publications. Section IV describes a range of systematics tests. We consider several sources of systematic errors in more detail in Sec. V, and redo fits in Sec. VI, where we present final results for $F_A(q^2)$. In Sec. VII we illustrate the propagation of errors to several derived observables, including the isovector axial nucleon radius and total neutrino-nucleon quasielastic cross sections. The incorporation of nucleon-level uncertainties in nuclear cross sections is illustrated with MINERvA data [56]. Section VIII provides a summary and conclusion.

II. DEUTERIUM DATA AND DIPOLE FITS

The world data from deuterium bubble chamber experiments consists of deuterium fills of the ANL 12-foot deuterium bubble chamber experiment [57–59], the BNL 7-foot deuterium bubble chamber experiment [60], and the FNAL 15-foot deuterium bubble chamber experiment [61]. We refer below to these experiments as ANL1982, BNL1981, and FNAL1983, respectively.[2]

A. Fits to Q^2 distributions

Extracting the axial form factor from data requires information about all other aspects of the scattering cross-section. The original publications used a variety of different inputs for axial (g_A) and magnetic ($\mu_p - \mu_n$) couplings, vector and pseudoscalar form factors, nuclear corrections, and muon mass corrections. Table I displays the input choices made in the original publications for each of the three considered data sets, as well as the updated inputs used for the remainder of this paper.[3]

The vector form factors are constrained by invoking isospin symmetry and constraints of electron-nucleon scattering data. In place of the Olsson vector form factors [63], we use the so-called BBA2005 parametrization that is commonly employed in contemporary neutrino studies [64]. Similar results were obtained using the BBA2003 [66] and BBBA2007 [67] parametrizations. Recent developments, connected with the so-called "proton radius puzzle," point to potential shortcomings in previous extractions of the vector form factors [35,68,69]. A systematic study of the vector form factors similar to the z expansion analysis of the axial form factor presented here is undertaken in Refs. [21,35].

For the pseudoscalar form factor F_P, we employ the partially conserved axial current (PCAC) ansatz,

$$F_P^{\mathrm{PCAC}}(q^2) = \frac{2m_N^2 F_A(q^2)}{m_\pi^2 - q^2}. \tag{1}$$

The free-nucleon form factors F_A and F_P are functions of the four momentum transfer q^2 from the lepton to the nucleon, and $m_N = 0.9389$ GeV, $m_\pi = 0.14$ GeV are the masses of the nucleon and the pion. The effects of the pseudoscalar form factor are suppressed in the limit of small lepton mass, and its uncertainties are negligible in most applications involving accelerator neutrino beams, including this analysis.

Nuclear corrections relating the free neutron cross section, $d\sigma^n$, to the deuteron cross section, $d\sigma^D$, may be parametrized as

$$\frac{d\sigma^D}{dQ^2} = R(Q^2, E_\nu)\frac{d\sigma^n}{dQ^2}, \tag{2}$$

where $d\sigma^D/dQ^2$ denotes the deuteron differential cross section with respect to the intrinsically positive $Q^2 = -q^2$.[4] The model of Ref. [65] was used in the original analyses, with $R(Q^2, E_\nu) \approx R(Q^2)$ independent of neutrino energy,

---

[1] Formalism for z expansion and nucleon form factors is described in Refs. [31,32], and several applications are found in Refs. [33–36]. Related formalism and applications may be found in [37–53].

[2] An updated BNL data set was presented in Ref. [62] with a factor ≈2 increase in number of events. However, we were unable to extract a sufficiently precise Q^2 distribution of events from this reference, since the data were presented on a logarithmic scale (cf. Ref. [62], Fig. 5) . We thus consider only the events from the BNL1981 data set.

[3] Form factor notations and conventions are as in Ref. [31].

[4] For definiteness in the deuteron case, we let Q^2 in Eq. (2) denote the leptonic momentum transfer. This definition is consistent with the experimental reconstruction, which assumed the kinematics for scattering from a free neutron in the presence of a spectator proton carrying opposite momentum to the neutron.

TABLE I. Inputs from the original publications, BNL1981 [60], ANL1982 [59], and FNAL1983 [61], and our default inputs. See text for details.

Input	BNL1981	ANL1982	FNAL1983	This work	Reference
$g_A = F_A(0)$	-1.23	-1.23	-1.23	-1.2723	[22]
$\mu_p - \mu_n - 1$	3.708	3.71	3.708	3.7058	[22]
F_{Vi}	Olsson [63]	Olsson [63]	Olsson [63]	BBA2005	[64]
F_P	PCAC	PCAC	PCAC	PCAC	(1)
Deuteron correction	Singh [65]	Singh [65]	Singh [65]	Singh	[65]
lepton mass	$m_\mu = m_\mu$ except ABC	$m_\mu = m_\mu$	$m_\mu = m_\mu$ except ABC	$m_\mu = m_\mu$	
Q^2 range	0.06–3 GeV^2	0.05–2.5 GeV^2	0–3 GeV^2		
N_{bins}	49	49	30		
N_{events}	1236	1792	354		
kinematic cut	$Q^2 \geq 0.06$ GeV^2	$Q^2 \geq 0.05$ GeV^2	$Q^2 \geq 0.10$ GeV^2		

and $R(Q^2) \to 1$ above $Q^2 \approx 0.2$ GeV^2. We retain this model as default, but examine deviations from this simple description below in Sec. IV, using the calculations of Ref. [70].

The neutrino-neutron quasielastic cross section may be written in a standard form

$$\frac{d\sigma^n}{dQ^2} \propto \frac{1}{E_\nu^2}\left[A(Q^2) \mp B(Q^2)\frac{s-u}{m_N^2} + C(Q^2)\frac{(s-u)^2}{m_N^4}\right], \qquad (3)$$

where $s - u = 4E_\nu m_N - Q^2 - m_\mu^2$ is the difference of Mandelstam variables, A, B and C are quadratic functions of nucleon form factors [71], and the vector-axial interference term B changes sign for the $\bar{\nu}p$ scattering process. In the BNL1981 and FNAL1983 data sets, the lepton mass was neglected inside the functions $A(Q^2)$, $B(Q^2)$, and $C(Q^2)$ of Eq. (3), but retained in other kinematic prefactors. In our analysis, we retain the complete lepton mass dependence.

The event distributions in Q^2 have been obtained by digitizing the relevant plots from the original publications. Table I gives the Q^2 range and bin size, the total number of events,[5] and the minimum Q^2 retained in the original analyses. In each case, events in a lowest Q^2 bin were omitted from fits, and only FNAL1983 reports these events. We retain the same binning and minimum Q^2 cut in our default fits. These distributions are included as Supplemental Material to the present paper [72].

B. E_ν distributions and flux

An advantage of the $\nu_\mu d \to \mu^- pp$ process in an exquisite device like a bubble chamber is the accurate reconstruction of the neutrino energy for each event. Cross section parameters can be constrained from the Q^2 distribution despite poorly controlled uncertainties in *ab initio* neutrino flux estimates. This is especially valuable for the low energy ANL1982 and BNL1981 data, whose neutrino energy spectrum significantly influences the shape of the dN/dQ^2 distribution through the energy-dependent kinematic limit corresponding to a backscattered lepton.

Unfortunately, event-level kinematics from the deuterium data sets are no longer available and unbinned likelihood fits using the E_ν and Q^2 dependence of the cross section cannot be repeated. However, the one-dimensional distribution of events in reconstructed neutrino energy, dN/dE_ν, may be extracted from the original publications, and we use this information to reconstruct the flux self-consistently. This subsection describes the procedure we use, including some subtle points required for later interpretation of the form factor fits.

The differential neutrino flux is determined by

$$\frac{d\Phi(E_\nu)}{dE_\nu} \propto \frac{1}{\sigma^n(E_\nu, F_A)}\frac{dN^n}{dE_\nu}, \qquad (4)$$

where $\sigma^n(E_\nu, F_A)$ is the free-neutron quasielastic cross section, and dN^n/dE_ν is the energy distribution of free-neutron events that would be obtained in the experimental flux. The constant of proportionality in Eq. (4) is determined by the number of target deuterons and the time duration of the experiment. Let us normalize the energy distribution according to

$$\int_0^\infty dE_\nu \frac{dN^n}{dE_\nu} = \mathcal{N}\int_{Q^2_{\mathrm{min}}}^\infty dQ^2 \frac{dN^D}{dQ^2}. \qquad (5)$$

Consistency in Eq. (5) is obtained when $\mathcal{N} = \hat{\mathcal{N}}(F_A, Q^2_{\mathrm{min}}, R)$, where

---

[5] For BNL1981 and ANL1982, the digitized number of events in each Q^2 bin was rounded to the nearest integer, resulting in the same total numbers, 1236 and 1792 respectively, quoted in the original publications. For FNAL1983, the digitization produced near-integer results in each Q^2 bin, but the total summed event number, 354, differs from the value 362 quoted in the original publication.

$$\hat{\mathcal{N}}(F_A, Q^2_{\mathrm{min}}, R) = \frac{\int_0^\infty dQ^2 \frac{dN^n}{dQ^2}}{\int_{Q^2_{\mathrm{min}}}^\infty dQ^2 \frac{dN^D}{dQ^2}}. \tag{6}$$

The right-hand side of Eq. (6) may be computed using a given dN^n/dE_ν, and depends on $R(Q^2, E_\nu)$ and $F_A(q^2)$ through Eqs. (2) and (4). Using the flux from Eq. (4), we have finally,

$$\left(\frac{dN^D}{dQ^2}\right)^{\mathrm{theory}} = \mathcal{N}_{\mathrm{fit}} \int_0^\infty dE_\nu \frac{R(Q^2,E_\nu)\frac{d\sigma^n}{dQ^2}(E_\nu,F_A,Q^2)}{\sigma^n(E_\nu,F_A)} \frac{dN^n}{dE_\nu}, \tag{7}$$

where a fit parameter, $\mathcal{N}_{\mathrm{fit}}$, has been introduced for the normalization.

Choosing $\mathcal{N} = \hat{\mathcal{N}}(F_A, Q^2_{\mathrm{min}}, R)$ in Eq. (5) would correspond to $\mathcal{N}_{\mathrm{fit}} = 1$. In order to avoid the explicit computation of the integrals (6), we instead take $\mathcal{N} = 1$, corresponding to the expectation $\mathcal{N}_{\mathrm{fit}} = \mathcal{N}(F_A, Q^2_{\mathrm{min}}, R)$. We allow the parameter $\mathcal{N}_{\mathrm{fit}}$ to float unconstrained in the fits, with an independent parameter for each experiment.

We emphasize that dN^n/dE_ν in Eq. (4) represents the energy distribution of free-neutron events that would be obtained in the experimental flux; this distribution is obtained from the energy distribution of observed events in deuterium by correcting for nuclear effects, for events lost due to the Q^2_{min} cut, and for other experimental effects. Such corrections were applied to the energy distribution presented in the BNL1981 data set, but not in the ANL1982 and FNAL1983 data sets. The effect of applying or not applying these corrections is found to be small, as discussed below in Sec. V A.

For later comparison, we compute the ratios (6) with a nominal dipole axial form factor [$m_A = 1$ GeV, cf. Eq. (9) below], neglecting deuteron corrections ($R = 1$), and at a nominal $E_\nu = 1$ GeV neutrino energy, for the Q^2_{min} values employed in the BNL1981, ANL1982, FNAL1983 data sets[6]:

$$\begin{aligned}
\hat{\mathcal{N}}(Q^2_{\mathrm{min}} &= 0.06\ \mathrm{GeV}^2) \approx 1.13, \\
\hat{\mathcal{N}}(Q^2_{\mathrm{min}} &= 0.05\ \mathrm{GeV}^2) \approx 1.11, \\
\hat{\mathcal{N}}(Q^2_{\mathrm{min}} &= 0.10\ \mathrm{GeV}^2) \approx 1.23.
\end{aligned} \tag{8}$$

We expect these numbers to be approximately reproduced in $\mathcal{N}_{\mathrm{fit}}$ when the deviation from $\hat{N} = 1$ in Eq. (6) is dominated by the Q^2_{min} cut.

Two further complications result in technical subtlety but do not affect the fit results. First, the binned event rate dN/dE_ν for ANL1982 is provided in a prior publication [73] that used a subset of about half the events. A second complication is the finite bin width of the dN/dE_ν distributions, which would yield unphysical discontinuities when displaying ANL and BNL dN/dQ^2 spectra at best fit. This effect is the result of convoluting a low energy flux with a differential cross section that has an energy-dependent kinematic limit. We use an interpolation algorithm to produce smoothed fluxes with 500 bins in energy over the original range of data. Nearly identical fit results are obtained regardless of whether the interpolation is a cubic spline, linear, or whether the original binning is used, so this step is primarily cosmetic. The smoothed and unsmoothed E_ν distributions are included as Supplemental Material to the present paper [72].

C. Dipole fits

Our results for the axial form factor will differ from the analyses in the original publications. These differences arise from a number of sources: updated numerical inputs in Table I; not using unbinned likelihood fits; and differences in axial form factor shape assumptions. In order to understand these differences, we begin by restricting attention to the dipole ansatz,

$$F_A^{\mathrm{dipole}}(q^2) = F_A(0)\left(1 - \frac{q^2}{m_A^2}\right)^{-2}, \tag{9}$$

and compare to fits in the original publications.

Table II gives results for fits to the dipole ansatz (9) for the axial form factor. The table shows "flux-independent" results from the original experiments, which performed unbinned likelihood fits to event-level data. Our results are from a Poisson likelihood fit to the binned Q^2 distribution of events obtained with a neutrino flux given by smoothing the binned reconstructed neutrino energy distribution (divided by theoretical cross section), as described in Sec. II B. Fits to the binned log-likelihood function are found by minimizing the function

$$-2\log[\mathcal{L}(F_A)] = 2\sum_i \left[\mu_i(F_A) - n_i + n_i \log\left(\frac{n_i}{\mu_i(F_A)}\right)\right], \tag{10}$$

TABLE II. Dipole axial mass extracted in original publications, our extraction using parameter inputs as in the original publications, and our extraction using updated constants and vector form factors as in Table I. Errors are statistical only.

	m_A^{dipole} (ref)	m_A^{dipole} (old)	m_A^{dipole} (new)
BNL 1981 [60]	1.07(6)	1.07(5)	1.05(5)
ANL 1982 [59]	1.05(5)	1.05(5)	1.02(5)
FNAL 1983 [61]	$1.05^{+0.12}_{-0.16}$	1.20(11)	1.17(10)

---

[6] While $E_\nu = 1$ GeV is close to the peak energy for the BNL1981 and ANL1982 data sets, the FNAL1983 data set involved higher energy. However, these ratios have mild energy dependence above $E_\nu \sim 1$ GeV, e.g. at $E_\nu = 10$ GeV the result is $\hat{\mathcal{N}}(Q^2_{\mathrm{min}} = 0.10\ \mathrm{GeV}^2) \approx 1.25$.

where n_i is the number of events in the ith bin, and μ_i is the theory prediction (7) for the bin. Errors correspond to changes of 1.0 in the -2LL function.

Because we do not use an unbinned likelihood fit, we do not expect precise agreement even when the original choices of constants in Table I are used. Comparing the first two columns of Table II, the size of the resulting statistical uncertainties are approximately equal, and only FNAL shows a discrepancy in central value. A similar exercise was performed in Refs. [66,74,75], and similar results were obtained. Having reproduced the original analyses to the extent possible, we will proceed with the updated constants as in the final column of Table I.

III. z EXPANSION ANALYSIS

The dipole assumption (9) on the axial form factor shape represents an unquantified systematic error. We now remove this assumption, enforcing only the known analytic structure that the form factor inherits from QCD. We investigate the constraints from deuterium data in this more general framework. A similar analysis may be performed using future lattice QCD calculations in place of deuterium data.

A. z expansion formalism

The axial form factor obeys the dispersion relation,

$$F_A(q^2) = \frac{1}{\pi}\int_{t_{\rm cut}}^{\infty} dt' \frac{{\rm Im} F_A(t'+i0)}{t'-q^2}, \tag{11}$$

where $t_{\rm cut} = 9m_\pi^2$ represents the leading three-pion threshold for states that can be produced by the axial current. The presence of singularities along the positive real axis implies that a simple Taylor expansion of the form factor in the variable q^2 does not converge for $|q^2| \geq 9m_\pi^2 \approx 0.18\ {\rm GeV}^2$. Consider the new variable obtained by mapping the domain of analyticity onto the unit circle [31],

$$z(q^2, t_{\rm cut}, t_0) = \frac{\sqrt{t_{\rm cut}-q^2} - \sqrt{t_{\rm cut}-t_0}}{\sqrt{t_{\rm cut}-q^2} + \sqrt{t_{\rm cut}-t_0}}, \tag{12}$$

where t_0, with $-\infty < t_0 < t_{\rm cut}$, is an arbitrary number that may be chosen for convenience. In terms of the new variable we may write a convergent expansion,

$$F_A(q^2) = \sum_{k=0}^{k_{\rm max}} a_k z(q^2)^k, \tag{13}$$

where the expansion coefficients a_k are dimensionless numbers encoding nucleon structure information.

In any given experiment, the finite range of Q^2 implies a maximal range for $|z|$ that is less than unity. We denote by $t_0^{\rm optimal}(Q^2_{\rm max})$ the choice which minimizes the maximum size of $|z|$ in the range $-Q^2_{\rm max} \leq q^2 \leq 0$. Explicitly,

TABLE III. Maximum value of $|z|$ for different Q^2 ranges and choices of t_0. $t_0^{\rm optimal}$ is defined in Eq. (14).

$Q^2_{\rm max}$ GeV^2	t_0	$\|z\|_{\rm max}$
1.0	0	0.44
3.0	0	0.62
1.0	$t_0^{\rm optimal}(1.0\ {\rm GeV}^2) = -0.28\ {\rm GeV}^2$	0.23
3.0	$t_0^{\rm optimal}(1.0\ {\rm GeV}^2) = -0.28\ {\rm GeV}^2$	0.45
3.0	$t_0^{\rm optimal}(3.0\ {\rm GeV}^2) = -0.57\ {\rm GeV}^2$	0.35

$$t_0^{\rm optimal}(Q^2) = t_{\rm cut}\left(1 - \sqrt{1 + Q^2_{\rm max}/t_{\rm cut}}\right). \tag{14}$$

Table III displays $|z|_{\rm max}$ for several choices of $Q^2_{\rm max}$ and t_0.

The choice of t_0 can be optimized for various applications. We have in mind applications with data concentrated below $Q^2 = 1\ {\rm GeV}^2$, and therefore take as default choice,

$$\bar{t}_0 = t_0^{\rm optimal}(1\ {\rm GeV}^2) \approx -0.28\ {\rm GeV}^2, \tag{15}$$

minimizing the number of parameters that are necessary to describe data in this region. Inspection of Table III shows that the form factor expressed as $F_A(z)$ becomes approximately linear. For example, taking $|z|_{\rm max} = 0.23$ implies that quadratic, cubic, and quartic terms enter at the level of ~5%, 1% and 0.3%.

The asymptotic scaling prediction from perturbative QCD [76], $F_A \sim Q^{-4}$, implies the series of four sum rules [35]

$$\sum_{k=n}^{\infty} k(k-1)\cdots(k-n+1)a_k = 0, \quad n = 0,1,2,3. \tag{16}$$

We enforce the sum rules (16) on the coefficients, ensuring that the form factor falls smoothly to zero at large Q^2. Together with the $Q^2 = 0$ constraint, this leaves $N_a = k_{\rm max} - 4$ free parameters in Eq. (13). From Eq. (16), it can be shown [35] that the coefficients behave as $a_k \sim k^{-4}$ at large k. We remark that the dipole ansatz (9) implies the coefficient scaling law $|a_k| \sim k$ at large k, in conflict with perturbative QCD.

In addition to the sum rules, an examination of explicit spectral functions and scattering data [31] motivates the bound of

$$|a_k/a_0| \leq 5. \tag{17}$$

As noted above, from Eq. (16), the coefficients behave as $a_k \sim k^{-4}$ at large k. We invoke a falloff of the coefficients at higher order in k,

$$|a_k/a_0| \leq 25/k, \quad k > 5. \tag{18}$$

The bounds are enforced with a Gaussian penalty on the coefficients entering the fit. We investigate fits using a range of k_{max}, other choices of t_0, and alternatives to Eqs. (17) and (18), which are briefly reported in Sec. IV.

B. z expansion basic fit results

Using the same data sets and constants as described in Sec. II and summarized in Table I, we perform fits replacing dipole axial form factor with z expansion as in Eq. (13). We use the scheme choice (15), enforce the sum rule constraints (16), and use the default bounds on the coefficients a_k in Eqs. (17), (18). The results are summarized in Table IV and displayed in Figs. 1 and 2. The coefficients corresponding to the fits with $N_a = 4$ free parameters in Table IV are

$$[a_1, a_2, a_3, a_4] = \begin{cases} [2.24(10), 0.6(1.0), -5.4(2.4), 2.2(2.7)] & \text{(BNL)} \\ [2.25(10), 0.2(0.9), -4.9(2.3), 2.7(2.7)] & \text{(ANL)}, \\ [2.02(14), -1.2(1.5), -0.7(2.9), 0.1(2.8)] & \text{(FNAL)} \end{cases} \tag{19}$$

where (symmetrized) errors correspond to a change of 1.0 in the -2LL function.

Table IV summarizes z expansion fits with different numbers of free parameters. Focusing on the first order coefficient,

$$[a_1(\text{BNL}), a_1(\text{ANL}), a_1(\text{FNAL})] = \begin{cases} [2.23(10), 2.23(10), 2.02(14)], & N_a = 3 \\ [2.24(10), 2.25(10), 2.02(14)], & N_a = 4. \\ [2.22(10), 2.25(10), 2.02(14)], & N_a = 5 \end{cases} \tag{20}$$

As discussed after Eq. (15), z^2, z^3, z^4, etc., terms in the z expansion become increasingly irrelevant, corresponding to $|z|_{\text{max}} \ll 1$ in Table III. This is borne out by the data, which determines a form factor with coefficients in Eq. (19) of order 1.0 that mostly do not push the Gaussian bounds, and a leading coefficient in Eq. (20) that is approximately the same regardless of whether terms beyond order z^3 are included.

The axial "charge" radius is defined via the form factor slope at $q^2 = 0$,

$$\frac{1}{F_A(0)} \frac{dF_A}{dq^2}\bigg|_{q^2=0} \equiv \frac{1}{6} r_A^2. \tag{21}$$

For a general scheme choice $t_0 \neq 0$, this quantity depends on all the coefficients in the z expansion. Table IV illustrates that r_A is poorly constrained without the restrictive dipole assumption. We will provide a final value for the axial radius from deuterium data after discussion of systematic errors in the next section.

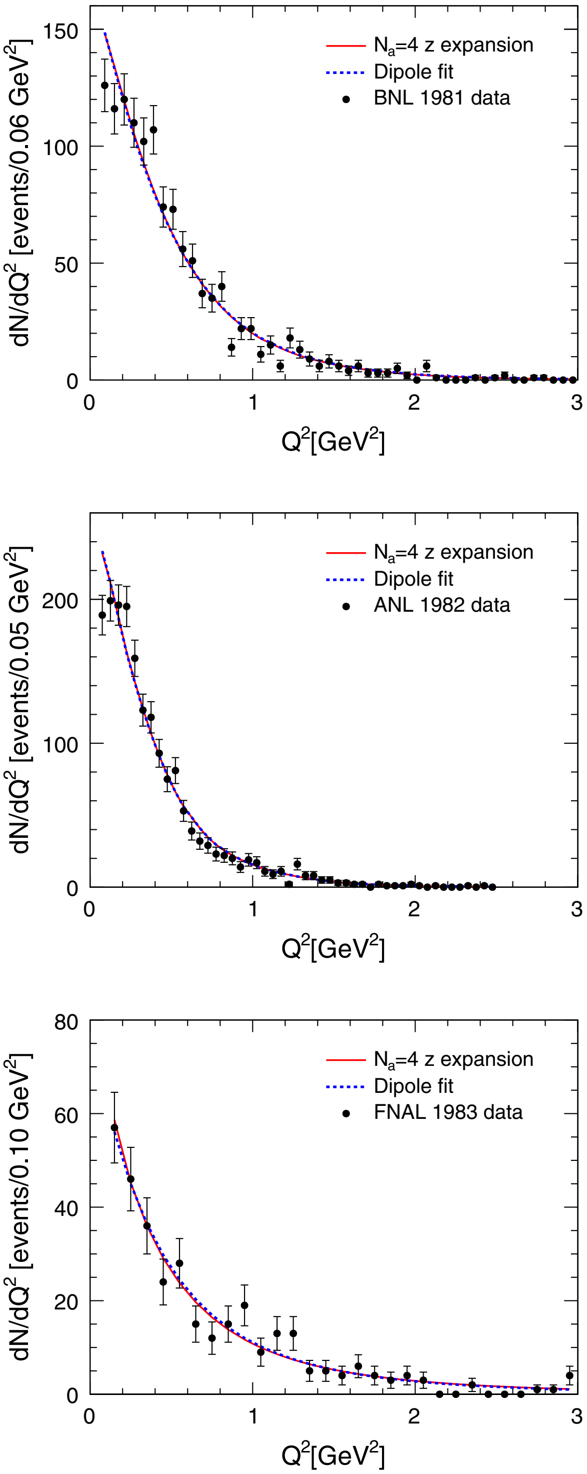

FIG. 1. Experimental data and best fit curves corresponding to dipole and $N_a = 4$ z expansion in Table IV, for BNL1981 (top pane), ANL1982 (middle pane) and FNAL1983 (bottom pane).

The normalization factor $\mathcal{N}_{\text{fit}}$ is also included in Table IV. This parameter is allowed to float without bounds, but returns values consistent with the approximation (8) to the expectation (6).

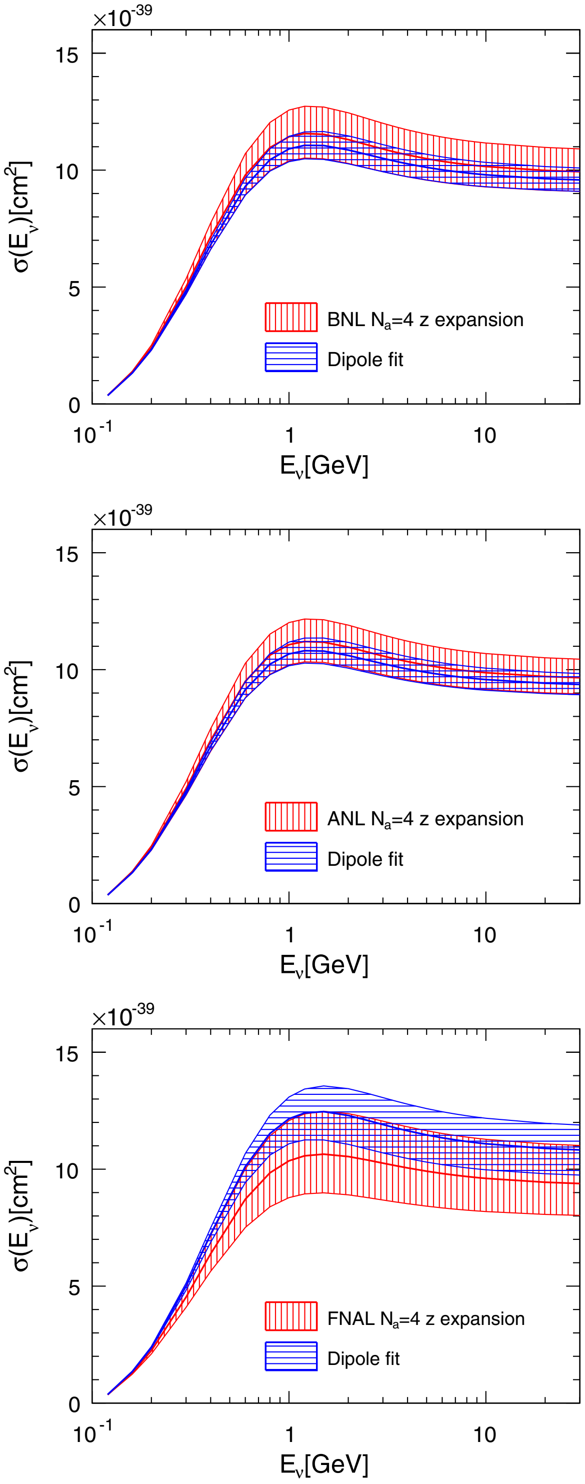

FIG. 2. Best fit curves and errors propagated from deuterium to free-neutron cross section, for BNL1981 (top pane), ANL1982 (middle pane) and FNAL1983 (bottom pane). Blue (horizontal stripes) corresponds to dipole and red (vertical stripes) to $N_a = 4$ z expansion in Table IV.

An interesting feature of the fits displayed in Fig. 1 is that whereas the best-fit dN/dQ^2 curves for dipole and z expansion are very similar in the considered Q^2 range, derived observables such as the radius in Table IV, and the absolutely normalized cross section in Fig. 2, can be markedly different. The presence of the Q^2_{min} cut, and the lack of an absolutely normalized flux, explains this situation, which is most apparent for FNAL1983. To illustrate, Fig. 3 shows the absolutely normalized $d\sigma^n/dQ^2$ computed using the central value dipole and z-expansion axial form factors for FNAL1983 in Figs. 1 and 2. Omitting the lowest-Q^2 data, and applying an overall normalization factor obscures the difference between these curves.

The normalization parameter $\mathcal{N}_{\mathrm{fit}}$ appearing in Eq. (7) is not externally constrained in our shape fits. The uncertainty after fitting yields $\sim \pm 10\%$ for BNL1981 and ANL1982 and $\sim \pm 20\%$ for FNAL1983, which is significantly larger than the ~3% to ~5% uncertainty from Poisson statistics. A simple Poisson constraint would not be adequate considering uncertainties from acceptance and deuterium corrections described later. A rate + shape fit with a correctly motivated uncertainty on $\mathcal{N}_{\mathrm{fit}}$ could in principle produce a somewhat better constrained form factor and cross section.

C. Residuals analysis

The best fits are still a relatively poor description of the data, apparent in both Table IV and Fig. 1. This was briefly discussed in the thesis [77] that accompanies the ANL1982 publication: the theoretical curve is too high at very low Q^2, becoming too low above 0.2 GeV^2, and too high again around 0.7 GeV^2. Similarly, the BNL1981 publication discusses the possibility of residual scanning biases with a kinematic dependence that mimics evidence for second-class currents violating the symmetries of QCD (cf. Ref. [60]). These observations motivate a careful examination of systematic uncertainties assigned in the fits.

The preference of the experiments for a common Q^2-dependent distortion can be illustrated by comparing the residual discrepancy between the data and the best fit curves from Fig. 1 in a single plot, shown in Fig. 4.[7] The distortion at lowest Q^2 is clearly significant. The data also seem to agree on potential distortions in the range $0.25 < Q^2 < 3.0$. However the null hypothesis, that the data in this range were drawn from a flat distribution, yields P-value of 0.12 and is not exceptional. In order to use a χ^2 fit for this P-value and to improve the plot readability, the upper bins in each data set were combined.

Form factors described by the z expansion, hence any form factor consistent with QCD, cannot accommodate such localized distortions of the Q^2 spectrum (the dipole ansatz similarly cannot accommodate such distortions). The $R(Q^2)$ model for deuterium used by the original

---

[7] For definiteness, the best fit curve is from a simultaneous fit to the BNL, ANL and FNAL data sets. A nearly identical plot is obtained if different best fit curves for each data set are used.

TABLE IV. Fits to z expansion using the same data and constants as the final column of Table II. "LL" denotes log likelihood. Errors on z expansion determinations of r_A^2 are determined from the error matrix, all others correspond to $\Delta(-2\mathrm{LL}) = 1$. $N_a = k_{\max} - 4$ denotes the number of free expansion coefficients in the z expansion fit (13) with scheme choice (15), sum rule constraints (16), and bounds (17), (18). The final column is the number of bins, including bins with zero data. For $N_a = 4$ the resulting fit parameters are displayed in Eq. (19).

	Dipole			$N_a = 3$			$N_a = 4$			$N_a = 5$			
Experiment	−2LL	$\mathcal{N}_{\rm fit}$	r_A^2 [fm^2]	−2LL	$\mathcal{N}_{\rm fit}$	r_A^2 [fm^2]	−2LL	$\mathcal{N}_{\rm fit}$	r_A^2 [fm^2]	−2LL	$\mathcal{N}_{\rm fit}$	r_A^2 [fm^2]	$N_{\rm bins}$
BNL1981	70.9	$1.14^{+0.08}_{-0.07}$	0.424(44)	76.1	$1.14^{+0.12}_{-0.11}$	0.36(21)	73.4	$1.13^{+0.13}_{-0.11}$	0.25(21)	71.0	$1.13^{+0.13}_{-0.12}$	0.18(21)	49
ANL1982	58.6	$1.15^{+0.06}_{-0.06}$	0.444(44)	62.3	$1.15^{+0.10}_{-0.09}$	0.38(19)	60.9	$1.14^{+0.10}_{-0.10}$	0.31(19)	59.9	$1.14^{+0.11}_{-0.10}$	0.27(19)	49
FNAL1983	38.2	$1.17^{+0.16}_{-0.13}$	0.337(61)	39.1	$1.21^{+0.24}_{-0.20}$	0.61(28)	39.1	$1.21^{+0.25}_{-0.21}$	0.60(28)	39.1	$1.20^{+0.26}_{-0.21}$	0.58(32)	29

experiments asymptotically approaches unity and also does not cause such distortions. It is interesting to consider whether more complete deuteron correction models, such as Ref. [70] (considered below in Fig. 6), could produce such distortions.[8] Finally, the impact of residual scanning biases should also be accounted for. In the next sections we turn to the question of assigning a systematic uncertainty to account for such effects.

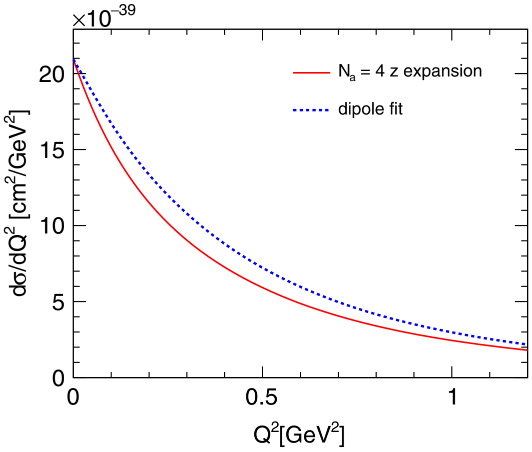

FIG. 3. Absolutely normalized $d\sigma^n/dQ^2$ at $E_\nu = 10$ GeV for dipole (blue) and z-expansion axial form factor central values as in the FNAL1983 results of Fig. 1 and Fig. 2.

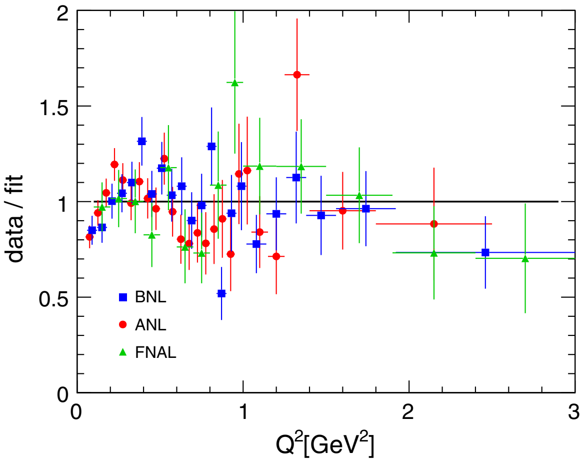

FIG. 4. Data divided by best fit prediction for the Q^2 distributions displayed in Fig. 1, for BNL (blue) ANL (red), and FNAL (green). Calculated $\chi^2/N_{\rm bins}$ are 35.3/22, 41.2/25, and 10.7/14 for BNL, ANL, and FNAL respectively.

IV. SYSTEMATIC TESTS

Fits using different choices for constructing the z expansion form factors should yield equivalent results for physical observables: a dependence on such choices would indicate an underestimated systematic uncertainty. Similarly, fits using different ranges of Q^2 should yield equivalent results.

A. Form factor scheme dependence

A test with variations of the number of free parameters was presented in Eq. (20) of the previous section. In order to translate other test fits into parameters that can be compared side-by-side, we will consider in all cases the dimensionless shape parameter defined by

$$\bar{a}_1 \equiv a_1|_{t_0=\bar{t}_0} \equiv -4(t_{\rm cut} - \bar{t}_0)F'_A(\bar{t}_0), \tag{22}$$

where $\bar{t}_0 \equiv t_0^{\rm optimal}(1\ \mathrm{GeV}^2) = -0.28\ \mathrm{GeV}^2$, as in Eq. (15). To motivate the choice (22), note that since z is a small parameter, the form factor is approximately linear when expressed as a function of z. The slope of this approximately linear function is the essential shape parameter determined by the data, and for convenience we define the slope at $q^2 = \bar{t}_0$. [The axial radius is similarly defined as the form factor slope at $q^2 = 0$ in Eq. (21).]

1. Magnitude of bound

Consider first the numerical value of the bound (17). For definiteness, we impose a coefficient falloff, $a_k \sim 1/k$, as in Eq. (18). Focusing on $N_a = 4$,

---

[8] Calculations of multinucleon effects for heavier nuclei like carbon exhibit qualitatively similar characteristics throughout this region of Q^2 [78,79].

TABLE V. Same as Table IV, but fitting only to data with $Q^2 \leq 1$ GeV^2. For $N_a = 4$ the resulting fit parameters are displayed in Eq. (25).

	Dipole			$N_a = 3$			$N_a = 4$			$N_a = 5$			
Experiment	-2LL	$\mathcal{N}_{\text{fit}}$	r_A^2 [fm^2]	-2LL	$\mathcal{N}_{\text{fit}}$	r_A^2 [fm^2]	-2LL	$\mathcal{N}_{\text{fit}}$	r_A^2 [fm^2]	-2LL	$\mathcal{N}_{\text{fit}}$	r_A^2 [fm^2]	N_{bins}
BNL1981	24.7	$1.16^{+0.08}_{-0.08}$	0.348(48)	27.2	$1.17^{+0.14}_{-0.13}$	0.32(22)	27.0	$1.17^{+0.14}_{-0.13}$	0.28(22)	26.6	$1.16^{+0.14}_{-0.13}$	0.24(22)	16
ANL1982	28.2	$1.14^{+0.07}_{-0.06}$	0.452(52)	31.7	$1.15^{+0.10}_{-0.09}$	0.38(19)	30.5	$1.14^{+0.10}_{-0.10}$	0.31(20)	29.2	$1.13^{+0.11}_{-0.10}$	0.24(20)	19
FNAL1983	8.3	$1.16^{+0.26}_{-0.18}$	0.33(12)	8.3	$1.22^{+0.29}_{-0.23}$	0.54(31)	8.2	$1.23^{+0.29}_{-0.24}$	0.56(29)	8.1	$1.24^{+0.30}_{-0.24}$	0.57(26)	9

TABLE VI. Same as Table IV, but fitting only to data with $Q^2 \geq 0.2$ GeV^2. For $N_a = 4$ the resulting fit parameters are displayed in Eq. (26).

	Dipole			$N_a = 3$			$N_a = 4$			$N_a = 5$			
Experiment	-2LL	$\mathcal{N}_{\text{fit}}$	r_A^2 [fm^2]	-2LL	$\mathcal{N}_{\text{fit}}$	r_A^2 [fm^2]	-2LL	$\mathcal{N}_{\text{fit}}$	r_A^2 [fm^2]	-2LL	$\mathcal{N}_{\text{fit}}$	r_A^2 [fm^2]	N_{bins}
BNL1981	60.7	$1.25^{+0.21}_{-0.14}$	0.61(13)	62.4	$1.28^{+0.20}_{-0.17}$	0.83(24)	61.5	$1.26^{+0.21}_{-0.18}$	0.74(25)	60.9	$1.25^{+0.23}_{-0.19}$	0.67(24)	47
ANL1982	43.2	$1.40^{+0.25}_{-0.38}$	$1.45^{+0.92}_{-0.49}$	45.8	$1.32^{+0.21}_{-0.18}$	1.04(24)	45.8	$1.32^{+0.23}_{-0.20}$	1.03(25)	45.8	$1.32^{+0.25}_{-0.21}$	1.05(24)	46
FNAL1983	38.2	$1.16^{+0.22}_{-0.16}$	0.33(7)	39.1	$1.22^{+0.31}_{-0.25}$	0.64(31)	39.1	$1.22^{+0.32}_{-0.25}$	0.63(30)	39.0	$1.21^{+0.34}_{-0.26}$	0.60(35)	28

$$[\bar{a}_1(\text{BNL}), \bar{a}_1(\text{ANL}), \bar{a}_1(\text{FNAL})] = \begin{cases} [2.18(8), 2.17(8), 2.01(12)], & |\frac{a_k}{a_0}| \leq \min(3, \frac{15}{k}) \\ [2.23(10), 2.25(10), 2.02(14)], & |\frac{a_k}{a_0}| \leq \min(5, \frac{25}{k}) \\ [2.36(15), 2.41(15), 2.02(17)], & |\frac{a_k}{a_0}| \leq \min(10, \frac{50}{k}) \end{cases}. \tag{23}$$

Results are consistent within errors. The very conservative bound $|a_k/a_0| \leq 10$ would lead to an error that is ~50% larger than our default $|a_k/a_0| \leq 5$.

2. Choice of t_0

Next, consider the choice of t_0.[9] A different choice of t_0 requires more parameters to achieve the same truncation error, $\sim|z|^{N_a+1}$. We compare the default case of $t_0 = -0.28$ GeV^2 and $N_a = 4$ to the case of $t_0 = 0$ and $N_a = 7$,[10] finding

$$[\bar{a}_1(\text{BNL}), \bar{a}_1(\text{ANL}), \bar{a}_1(\text{FNAL})] = \begin{cases} [2.24(10), 2.25(10), 2.02(14)] & (N_a = 4, t_0 = \bar{t}_0) \\ [2.22(9), 2.21(10), 2.02(14)] & (N_a = 7, t_0 = 0) \end{cases}, \tag{24}$$

where the errors are propagated using the covariance matrix for the coefficients a_k. Nearly identical results are obtained for different choices of t_0.

B. Subsets of the Q^2 range

A nonstatistical scatter of data points about the best fit curves is apparent in Fig. 1, and indicated by the poor fit quality in Table IV. Removing subsets of the data at high or low Q^2 will help isolate sources of tension between data and fit.

First, consider the removal of high Q^2 data, fitting to bins whose center is within the restricted range $Q^2 \leq 1$ GeV^2. The analog of Table IV for this case is given by Table V. Figure 5 shows comparisons of best fit curves and data points. The analog of Eq. (19) is

$$[a_1, a_2, a_3, a_4]|_{Q^2 \leq 1\,\text{GeV}^2} = \begin{cases} [1.99(15), 0.5(1.1), -3.6(2.6), 1.1(2.7)] & (\text{BNL}) \\ [2.29(14), 0.2(0.9), -5.2(2.5), 2.9(2.7)] & (\text{ANL}) \\ [1.88(25), -0.9(1.6), -0.3(2.9), -0.3(2.8)] & (\text{FNAL}) \end{cases}. \tag{25}$$

The omission of low-Q^2 data has a similarly large effect on the fit parameters. Fitting to the range $Q^2 \geq 0.2$ GeV^2, the results are given in Table VI. The z expansion coefficients are determined for $N_a = 4$ to be

$$[a_1, a_2, a_3, a_4]|_{Q^2 \geq 0.2\,\text{GeV}^2} = \begin{cases} [2.35(10), -2.0(1.2), -1.4(2.8), 1.4(2.7)] & (\text{BNL}) \\ [2.34(10), -3.6(1.2), 1.6(2.8), 0.9(2.8)] & (\text{ANL}) \\ [2.04(16), -1.3(1.6), -0.5(3.0), 0.1(2.8)] & (\text{FNAL}) \end{cases}. \tag{26}$$

Comparing the results in Tables IV, V, and VI and in Eqs. (19), (25), and (26), we see that the leading a_1 and a_2

---

[9] For $t_0 = t_0^{\text{optimal}}(1\ \text{GeV}^2) = -0.28$ GeV^2, by design, the shape parameter is identified with the linear coefficient of the z expansion in Eq. (13). Since $\bar{a}_1$ [Eq. (22)] is a physical observable, it can be computed for any choice of $t_0 \neq \bar{t}_0$.

[10] Both cases have $|z|_{\max}^{N_a+1} \approx 0.02$ in the range $0 < Q^2 < 3\,\text{GeV}^2$.

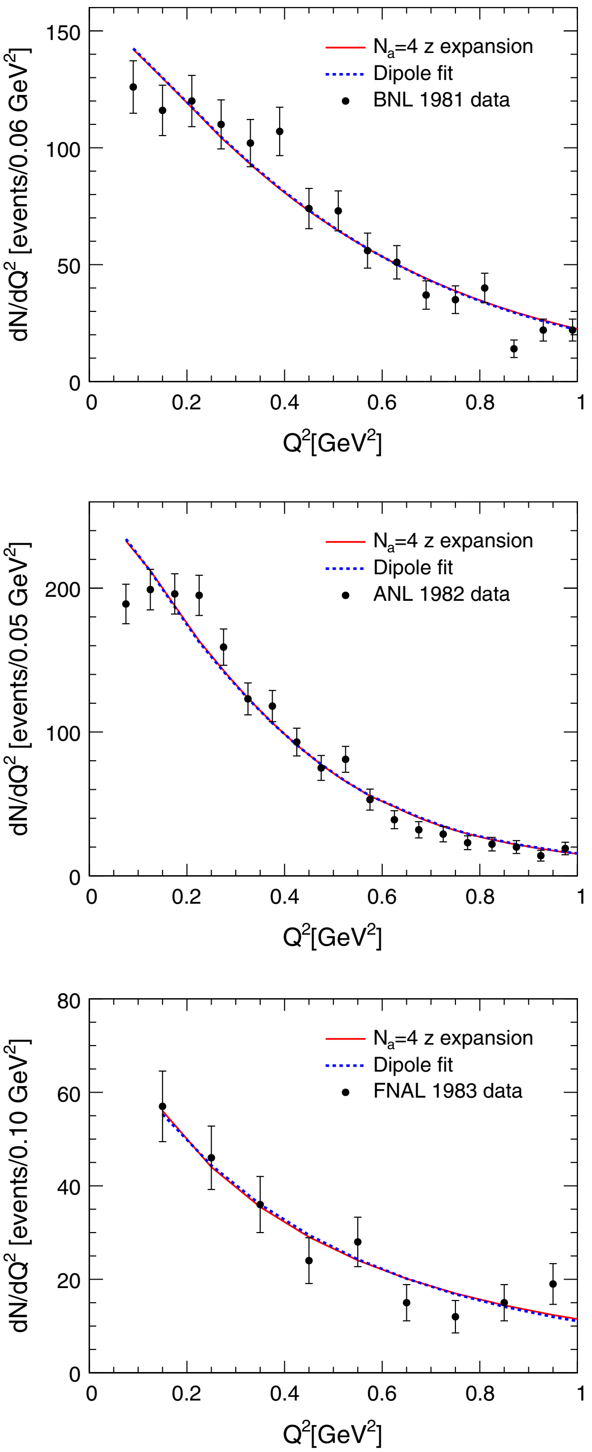

FIG. 5. Same as Fig. 1, but with $Q^2 \leq 1\ \mathrm{GeV}^2$. These fits correspond to the $N_a = 4$ z expansion in Table V.

parameters shift in some cases by about twice the statistical uncertainty of the fits. This reflects how different parts of the Q^2 range contribute to tensions in the fit. The minimum value of $-2\mathrm{LL} \sim \chi^2$ decreases in both cases, closer to a range that would be considered an adequate description of the data. The improvement when eliminating the low-Q^2 region is especially striking considering it amounts to only two or three bins of data in each data set.

One method to translate the tensions in the fit to an uncertainty on the fit parameters is to consider what additional error is necessary to obtain a reduced χ^2 of unity. We include an error for each data point proportional to the number of events in the original dN/dQ^2 distribution. This requires the use of a χ^2 calculation instead of a log-likelihood fit, which we achieve by limiting the test to the sample with $Q^2 \leq 1\ \mathrm{GeV}^2$. Adding this error in quadrature to the statistical error, we see that for BNL, an additional 10% error is required, while ANL requires an additional 7.5% error.

V. SYSTEMATIC ERRORS

The experimental uncertainties in the fits summarized in Table IV correspond only to statistical errors on the number of events in each bin. With a framework in place to quantify theoretical form factor shape uncertainty, let us examine several sources of systematic error, and their impact on the extraction of F_A.

Experimental systematic uncertainties come from the construction of the neutrino flux, and from acceptance corrections. A theoretical systematic error arises from uncertain modeling of deuteron effects.

A. Flux

Our procedure includes a self-consistent determination of the neutrino flux for fits to the Q^2 distributions, as described in Sec. II B. Systematic uncertainty estimates in the experimenter's *ab initio* flux do not apply. Instead we check for sensitivity to fluctuations in the number of events by varying one dN/dE_ν bin by its statistical error, reextracting fit parameters, and then repeating for all bins. Adding errors in quadrature, the result for the BNL data set is

$$\bar{a}_1 = 2.24 \pm 0.10_{\mathrm{stat}\,Q^2} \pm 0.04_{\mathrm{stat}\,E_\nu} \quad (\mathrm{BNL1981}). \tag{27}$$

Such an additional flux error is numerically subleading compared to statistical error, and also to the systematic error assigned below to account for deuteron and acceptance corrections. We neglect it in our final fits.

The consistency of the flux procedure could also be impacted by distortions of the dN/dE_ν distribution by Q^2_{min} cuts or deuteron corrections. Recall that the energy distribution from BNL1981, but not from ANL1982 or FNAL1983, was corrected for these effects. We have checked that the resulting variations are even smaller than the statistical fluctuations in Eq. (27), and are neglected.

B. Acceptance corrections

One source of uncertainty, especially in the limit of very low Q^2, is the acceptance corrections associated with human-eye scanning of the bubble chamber photographs. For example, Fig. 1 of ANL 1982 [59] provides an estimate of the scanning efficiency ranging from $e = 90 \pm 7\%$ at $0.05\ \mathrm{GeV}^2 < Q^2 < 0.1\ \mathrm{GeV}^2$ to $e = 98 \pm 1\%$ for $Q^2 > 0.15\ \mathrm{GeV}^2$. We include a possible correlated efficiency correction by making the following replacement in the efficiency-corrected number of events:

$$\frac{dN}{e(Q^2)} \to \frac{dN}{e(Q^2) + \eta de(Q^2)} = \frac{dN}{e(Q^2)}\left(1 + \eta\frac{de(Q^2)}{e(Q^2)}\right)^{-1}. \tag{28}$$

Here $\eta = 0 \pm 1$ is a parameter introduced in the fit, and we use a simple linear interpolation of the function in Ref. [59] for the efficiency $e(Q^2)$ and efficiency error $de(Q^2)$.

In the BNL data set, an efficiency effect with similar magnitude is presented, but not directly in the Q^2 variable. For simplicity we take the ANL function to represent possible effects also in the BNL and FNAL data sets, with independent floating scale parameters $\eta = 0 \pm 1$ in Eq. (28). The shape parameters and minimum $-2\mathrm{LL}$ values are as follows, comparing results with and without the acceptance correction,

$$\mathrm{BNL}:\ [\bar{a}_1, -2\mathrm{LL}] = \begin{cases} [1.99(15), 27.0] & (\text{without}) \\ [2.04(15), 26.0] & (\text{with}) \end{cases},$$
$$\mathrm{ANL}:[\bar{a}_1, -2\mathrm{LL}] = \begin{cases} [2.29(14), 30.5] & (\text{without}) \\ [2.38(14), 26.3] & (\text{with}) \end{cases},$$
$$\mathrm{FNAL}:[\bar{a}_1, -2\mathrm{LL}] = \begin{cases} [1.88(25), 8.2] & (\text{without}) \\ [1.88(25), 8.2] & (\text{with}) \end{cases}. \tag{29}$$

The parameter η takes on values of -1.9, -1.0, and $+0.01$ for data from ANL1982, BNL1981, and FNAL1983 respectively; the negative values indicate a pull to decrease the predicted cross section to match the data. In each case there is only modest improvement in the fit quality, and small impact on the form factor shape. Acceptance corrections within the quoted range have only minor impact.

C. Deuteron corrections

The analysis to this point, like the original analyses, used the deuteron correction model $R(Q^2)$ of Singh [65]. This model yields a suppression of the cross section for $Q^2 < 0.16\ \mathrm{GeV}^2$.[11] An example of a modern calculation with extended range in energy and Q^2 is given by Shen *et al.* in Ref. [70].[12] The Shen *et al.* model is overlaid with the original Singh model as well as the free neutron model in Fig. 6. The Shen *et al.* model deviates substantially from the free-neutron result at the ~20% level over a broad Q^2 range. These models do not constitute an estimate of the uncertainty on deuteron corrections, but suggest an avenue for future work even if there are no future measurements on deuterium.

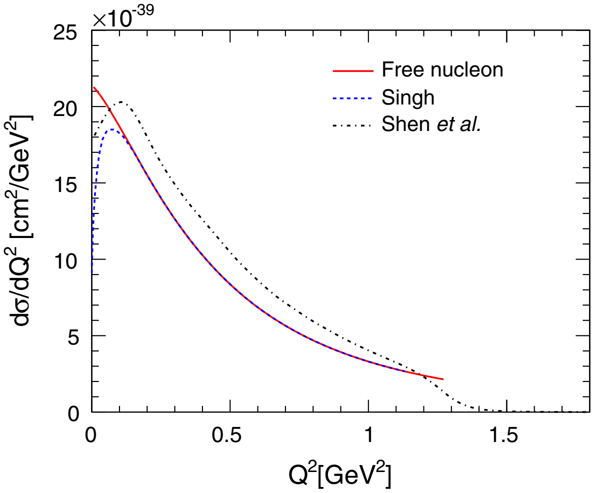

FIG. 6. Differential scattering cross sections for neutrino-deuteron scattering at 1 GeV neutrino energy, employing different nuclear models. The solid (red) curve is the free-neutron result. The dashed (blue) curve is obtained from the free-neutron result using the model from Ref. [65], as in the original deuterium analyses. The top dot-dashed (black) curve is extracted at $E_\nu = 1$ GeV from Ref. [70]. The charged lepton mass is neglected in this plot.

Assuming an energy independent, but Q^2 dependent, deuteron correction, the change in the fit results can be compared. For illustration, we employ the results of Ref. [70] at $E_\nu = 1\,\mathrm{GeV}$, and limit attention to $Q^2 \leq 1\,\mathrm{GeV}^2$, i.e., the configuration of Table V and Eq. (25). Shape parameter and minimum $-2\mathrm{LL}$ values are

$$\mathrm{BNL}:[\bar{a}_1, -2\mathrm{LL}] = \begin{cases} [1.99(15), 27.0] & (\text{Singh}) \\ [2.16(14), 25.1] & (\text{Shen et al.}) \end{cases},$$
$$\mathrm{ANL}:[\bar{a}_1, -2\mathrm{LL}] = \begin{cases} [2.29(14), 30.5] & (\text{Singh}) \\ [2.46(13), 29.2] & (\text{Shen et al.}) \end{cases},$$
$$\mathrm{FNAL}:[\bar{a}_1, -2\mathrm{LL}] = \begin{cases} [1.88(25), 8.2] & (\text{Singh}) \\ [2.00(25), 9.1] & (\text{Shen et al.}) \end{cases}. \tag{30}$$

The extracted form factor shifts to mimic the difference in the curves in Fig. 6, and there is slight improvement in fit quality for two of the three data sets.

D. Final systematic error budget

The most important systematic uncertainties are the two that significantly modify the Q^2 distribution: acceptance corrections and the deuteron correction. In our final

---

[11] A follow-up analysis [80] considers effects of meson exchange currents and alternate deuteron wave functions, with a total result very similar to Ref. [65].

[12] See also Ref. [81].

analysis, we modify the original fits displayed in Table V. First, we allow a correlated acceptance correction as in Eq. (28). Second, we include a 10% error added in quadrature to statistical error in each Q^2 bin to account for residual deuteron or other systematic corrections, as described at the end of Sec. IV B. With these corrections in place, we perform a χ^2 fit to all data up to $Q^2 = 1\ \mathrm{GeV}^2$. The neglect of data above $Q^2 = 1\ \mathrm{GeV}^2$ has only minor impact on the extraction of $F_A(q^2)$, and allows a simple treatment of these combined uncertainties with full covariance using a χ^2 fit.

As an alternative, we also provide a log-likelihood fit to the data up to $Q^2 = 3\ \mathrm{GeV}^2$, but without inflated errors to account for deuterium and other residual systematics. This has the benefit of including data over the entire kinematic range, but omits sources of systematic error that would need to be treated separately.

VI. AXIAL FORM FACTOR EXTRACTION

The best axial form factor is extracted from a joint fit to the three data sets. We choose $N_a = 4$ free parameters with $t_0 = t_0^{\mathrm{optimal}}(1\ \mathrm{GeV}^2)$ and data with $Q^2 \le 1\ \mathrm{GeV}^2$. As discussed above, this corresponds to a $k_{\max} = 8$ z expansion, where five linear combinations of coefficients are fixed by the $Q^2 = 0$ constraint and by the four sum rules (16). The acceptance correction free parameter is independent for each experiment in the joint fit.

Our knowledge of the axial form factor resulting from deuterium scattering data is summarized by constraints on the coefficients a_k. Central values and 1σ errors determined from $\Delta\chi^2 = 1$ are[13]

$$[a_1, a_2, a_3, a_4] = [2.30(13), -0.6(1.0), -3.8(2.5), 2.3(2.7)]. \tag{31}$$

The diagonal entries of the error (covariance) matrix, computed from the inverse of the Hessian matrix for $\chi^2(\{a_k\})$, are

$$E_{\mathrm{diag}} = [0.0154, 1.08, 6.54, 7.40]. \tag{32}$$

Note that $(E_{\mathrm{diag}})_i \approx (\delta a_i)^2$, reflecting approximately Gaussian behavior. The four-dimensional correlation matrix is

$$C_{ij} = \begin{pmatrix} 1 & 0.350 & -0.678 & 0.611 \\ 0.350 & 1 & -0.898 & 0.367 \\ -0.678 & -0.898 & 1 & -0.685 \\ 0.611 & 0.367 & -0.685 & 1 \end{pmatrix} \tag{33}$$

and as usual the error matrix is given by $E_{ij} = \delta a_i \delta a_j C_{ij}$. This description can be systematically improved when and if further data or externally constrained deuterium models become available. The form factor is plotted versus Q^2 and versus z in Fig. 7, and compared with a previous world average dipole form factor from Ref. [55].

We also provide an alternate log-likelihood determination of the axial form factor to the range $Q^2 < 3.0\ \mathrm{GeV}^2$, but without deuteron systematic corrections. Central values and 1σ errors determined from $\Delta(-2LL) = 1$ are

$$[a_1, a_2, a_3, a_4] = [2.28(8), 0.25(95), -5.2(2.3), 2.6(2.7)]. \tag{34}$$

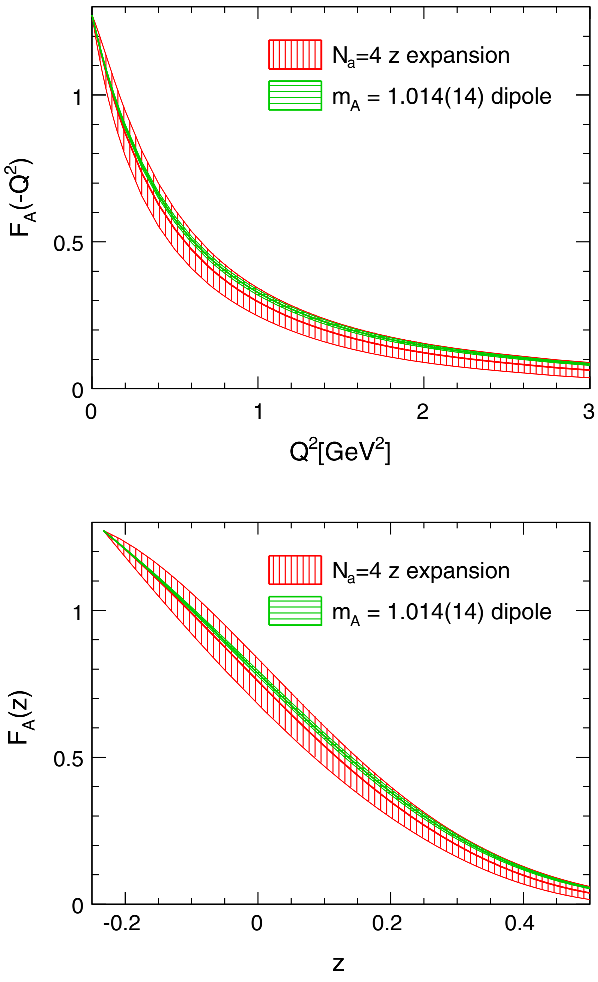

FIG. 7. Final form factor from Eqs. (31), (32) and (33). Also shown is the dipole axial form factor with axial mass $m_A = 1.014(14)$ GeV [55].

---

[13] The complete specification for the form factor involves the normalization $g_A = -1.2723$ from Table I; the pion mass $m_\pi = 0.14$ GeV employed in the specification of $t_{\mathrm{cut}} = 9m_\pi^2$ in Eq. (12); and the choice $t_0 = -0.28\ \mathrm{GeV}^2$. The remaining coefficients, a_0, a_5, a_6, a_7 and a_8, are determined by $F_A(0) = g_A$, and by the sum rule constraints (16); for ease of comparison we list the complete list of central values here: $[a_0, \ldots, a_8] = [-0.759, 2.30, -0.6, -3.8, 2.3, 2.16, -0.896, -1.58, 0.823]$.

The diagonal entries of the error matrix are

$$E_{\mathrm{diag}} = [0.00635, 0.781, 4.49, 6.87], \tag{35}$$

and the four-dimensional correlation matrix is

$$C_{ij} = \begin{pmatrix} 1 & 0.321 & -0.677 & 0.761 \\ 0.321 & 1 & -0.889 & 0.313 \\ -0.677 & -0.889 & 1 & -0.689 \\ 0.761 & 0.313 & -0.689 & 1 \end{pmatrix}. \tag{36}$$

VII. APPLICATIONS

Having presented the axial form factor with errors and correlations amongst the coefficients, we may systematically compute derived observables that depend on this function. We consider several applications of our results.

A. Axial radius

We begin with the axial radius, defined in Eq. (21). While the radius by itself is not the only quantity of interest to neutrino scattering observables, it is only through the $q^2 \to 0$ limit that a robust comparison can be made to other processes such as pion electroproduction.

The form factor coefficients and error matrix from the χ^2 fit in Sec. VI determine the radius as

$$r_A^2 = 0.46(22)\ \mathrm{fm}^2. \tag{37}$$

The constraint is much looser than would be obtained by restricting to the dipole model, cf. Table IV.[14] For comparison, let us consider the constraints from individual experiments. Table VII gives results for $N_a = 3$, 4, 5 free parameters, with errors determined from the error matrix in Eqs. (32) and (33). The results from individual experiments are consistent with the joint fit. Note that the joint fit is not simply the average of the individual fits. This situation arises from a slight tension between data and Gaussian coefficient constraints (17) when comparing a single data set to the statistically more powerful combined data.

B. Neutrino-nucleon quasielastic cross sections

Current and future neutrino oscillation experiments will precisely measure neutrino mixing parameters, determine the neutrino mass hierarchy, and search for possible *CP* violation and other new phenomena. This program relies on accurate predictions, with quantifiable uncertainties, for neutrino interaction cross sections. As the simplest examples, consider the charged-current quasielastic cross section $\sigma(E_\nu)$ for neutrino (antineutrino) scattering on an isolated neutron (proton).

TABLE VII. Axial radius extracted using best values from Table I, and default priors as discussed in the text. Note that the joint fit is not an average, but a simultaneous fit to all of the data sets.

Data set	r_A^2 [fm^2] ($N_a = 3$)	r_A^2 [fm^2] ($N_a = 4$)	r_A^2 [fm^2] ($N_a = 5$)
BNL 1981	0.56(23)	0.52(25)	0.48(26)
ANL 1982	0.69(21)	0.63(23)	0.57(24)
FNAL 1983	0.63(34)	0.64(35)	0.64(35)
Joint Fit	0.54(20)	0.46(22)	0.39(23)

The best fit cross section and uncertainty are shown in Fig. 8, and compared to the prediction of dipole F_A with axial mass $m_A = 1.014(14)$ [55]. At representative energies, the cross sections and uncertainties shown in Fig. 8 are

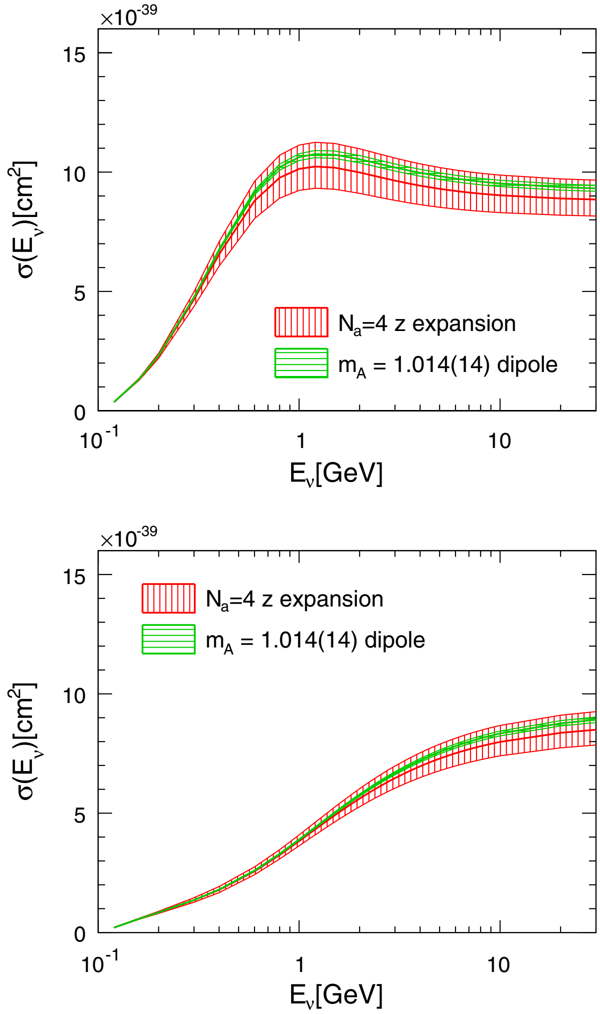

FIG. 8. Free nucleon CCQE cross section computed from Eqs. (31), (32) and (33), for neutrino-neutron (top) and antineutrino-proton (bottom) scattering. Also shown are results using dipole axial form factor with axial mass $m_A = 1.014(14)$ GeV [55].

---

[14] Extractions of the radius from electroproduction data are also strongly influenced by the dipole assumption [31].

$$\sigma_{\nu n\to\mu p}(E_\nu = 1\ \mathrm{GeV}) = 10.1(0.9)\times 10^{-39}\ \mathrm{cm}^2,$$
$$\sigma_{\nu n\to\mu p}(E_\nu = 3\ \mathrm{GeV}) = 9.6(0.9)\times 10^{-39}\ \mathrm{cm}^2, \qquad (38)$$

for neutrinos and

$$\sigma_{\bar\nu p\to\mu n}(E_\nu = 1\ \mathrm{GeV}) = 3.83(23)\times 10^{-39}\ \mathrm{cm}^2,$$
$$\sigma_{\bar\nu p\to\mu n}(E_\nu = 3\ \mathrm{GeV}) = 6.47(47)\times 10^{-39}\ \mathrm{cm}^2, \qquad (39)$$

for antineutrinos.

C. Neutrino nucleus cross sections

Connecting nucleon-level information to experimentally observed neutrino-nucleus scattering cross sections requires data-driven modeling of nuclear effects. Our description of the axial form factor and uncertainty in Eqs. (31), (32), and (33) can be readily implemented in neutrino event generators that interface with nuclear models.[15]

A multitude of studies and comparisons are possible. As illustration, consider MINERvA quasielastic data on carbon [56]. Figure 9 shows a comparison of the Q^2 distribution of measured events with the predictions from our $F_A(q^2)$, using a relativistic Fermi gas nuclear model in the default configuration of the GENIE v2.8 neutrino event generator [6]. For comparison, we display the result obtained using a dipole F_A with axial mass central value and error as quoted in the world average of Ref. [55]. The central curves differ in their kinematic dependence, and the dipole result severely underestimates the uncertainty propagated from deuterium data.

The z expansion implementation within GENIE includes a complete description of parameter errors and correlations. This will provide a systematic approach for testing different nuclear models and fitting nuclear model parameters, and for propagating uncertainties in nucleon-level amplitudes through to oscillation observables.

D. Discussion

The dipole ansatz has been commonly used to parametrize the axial form factor in neutrino cross section predictions. The axial mass parameter in this ansatz often appears with either a very small uncertainty, e.g. $m_A = 1.014(14)$ GeV [55], or a very large uncertainty, e.g. $m_A = 1.21(45)$ GeV [14].

In the first case, the small error estimate results from the restrictive dipole ansatz, and is likely an underestimate of the actual uncertainty: as a point of comparison, the $\lesssim 1.5\%$ axial radius error is comparable to or smaller than the uncertainty on the proton charge radius [35,69]. Recall that the charge radius is defined for the vector charge form factor analogously to the axial radius for the axial form factor. In contrast to the axial radius from neutrino-deuteron scattering, the charge radius from electron-proton scattering involves much *higher* statistics, a *monoenergetic* beam, and a *simpler*, proton, target.

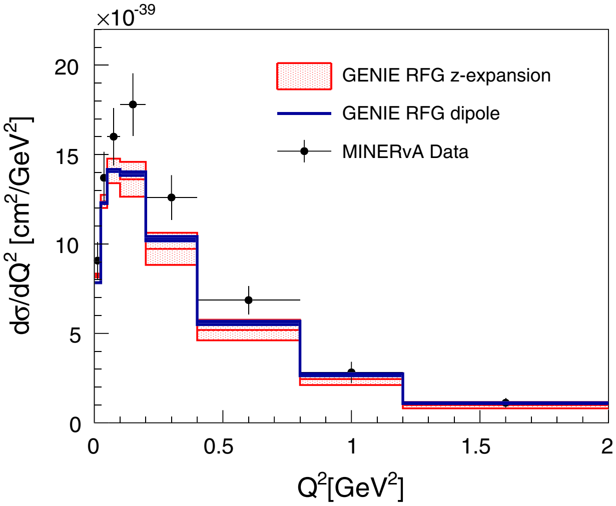

FIG. 9. Cross section for charged-current quasielastic events from the MINERvA experiment [56] as a function of reconstructed Q^2, compared with prediction using relativistic Fermi gas (RFG) nuclear model with z expansion axial form factor extracted from deuterium data. MINERvA data uses an updated flux prediction from [82]. Also shown are results using the same nuclear model but dipole form factor with axial mass $m_A = 1.014(14)$ GeV [55].

In the second case, the large uncertainty on m_A is typically included to account for tensions in external inputs from other experiments [14], and/or poorly constrained nuclear effects. Neither of these approaches is suited to the kinds of analyses that can be undertaken with modern cross section data such as the MINERvA example considered in Fig. 9. Underestimating nucleon-level uncertainties will bias conclusions about neutrino parameters or nuclear models. Inflating errors on m_A within a dipole ansatz fails to capture the correct kinematic dependence of either nucleon-level uncertainties, or of nuclear corrections.[16]

VIII. SUMMARY AND CONCLUSION

The constraints of elementary target data are critical to precision neutrino-nucleus cross sections underlying the accelerator neutrino program. Oscillation experiments rely on event rate predictions using nucleon-level amplitudes corrected for nuclear effects. Cross section experiments on nuclear targets can measure these nuclear effects but a

---

[15] The z expansion will be available in GENIE production release v2.12.0. The code is currently available in the GENIE trunk prior to its official release. The module provides full generality of the z expansion, and supports reweighting and error analysis with correlated parameters.

[16] Nondipole parametrizations have been considered in Refs. [67,83]. Similar remarks apply to these examples.

complete accounting of uncertainty in nucleon-level amplitudes is critical for disentangling nucleon-level, nuclear-level, and flux uncertainties, and for determining final sensitivity to fundamental neutrino parameters.

The axial form factor is a prominent source of nucleon-level uncertainty. We have analyzed the world data set for quasielastic neutrino-deuteron scattering using a model-independent description of the axial form factor. Our final results are presented with central values (31), errors (32), and correlations (33). Any observable depending on the axial form factor may be computed from these results, with a complete error budget.

The axial radius, governing the shape of the axial form factor, is presented in Eq. (37). It has a significantly larger uncertainty than previously estimated based on the unjustified dipole ansatz. Benchmark total cross sections on nucleon targets are presented in Fig. 8 and Eqs. (38) and (39). The incorporation of nuclear effects with the RFG model is illustrated in Fig. 9.

The form factor and uncertainty budget presented here are important new inputs to the neutrino cross section effort. It is interesting to investigate potential impacts and interplay with a variety of other processes such as neutrinoless double beta decay matrix elements [84,85] and the muon capture rate in muonic hydrogen [30]. The methodology presented can be revised or extended if new information becomes available. Future hydrogen or deuterium data would be trivial to include. Updated calculations for neutrino-deuteron scattering, especially if accompanied by an uncertainty, can be readily incorporated on top of this result. Lattice QCD holds promise to determine the axial form factor over much of the relevant Q^2 range, in a manner that is free from nuclear corrections [86–91].

ACKNOWLEDGMENTS

We thank L. Alvarez Ruso, J. R. Arrington, H. Budd, S. Bacca, A. Kronfeld, T. Mann, J. Morfin, G. Paz, and J. W. Van Orden for discussions, and R. Schiavilla for providing data files and interpretation of the results of Ref. [70]. R. G. was supported by NSF Grant No. 1306944. Research of R. J. H. and A. S. M. was supported by DOE Grant No. DE-FG02-13ER41958. R. G. and R. J. H. thank CETUP* (Center for Theoretical Underground Physics and Related Areas) for its hospitality and partial support during the 2014 Summer Program. Research of A. S. M. was also supported by the U.S. Department of Energy, Office of Science Graduate Student Research (SCGSR) program. The SCGSR program is administered by the Oak Ridge Institute for Science and Education for the DOE under Contract No. DE-AC05-06OR23100.

---

[1] R. Acciarri *et al.* (DUNE Collaboration), Long-Baseline Neutrino Facility (LBNF) and Deep Underground Neutrino Experiment (DUNE) conceptual design report, Volume 2: The Physics Program for DUNE at LBNF, arXiv:1512.06148.
[2] Y. Itow *et al.* (T2K Collaboration), The JHF-Kamioka neutrino project, arXiv:hep-ex/0106019.
[3] P. Adamson *et al.* (NOvA Collaboration), First measurement of electron neutrino appearance in NOvA, Phys. Rev. Lett. **116**, 151806 (2016).
[4] P. Adamson *et al.* (NOvA Collaboration), First measurement of muon-neutrino disappearance in NOvA, Phys. Rev. D **93**, 051104 (2016).
[5] H. Chen *et al.* (MicroBooNE Collaboration), Report No. FERMILAB-PROPOSAL-0974.
[6] C. Andreopoulos *et al.*, The GENIE neutrino Monte Carlo generator, Nucl. Instrum. Methods Phys. Res., Sect. A **614**, 87 (2010).
[7] Y. Hayato, A neutrino interaction simulation program library NEUT, Acta Phys. Polon. B **40**, 2477 (2009).
[8] O. Buss, T. Gaitanos, K. Gallmeister, H. van Hees, M. Kaskulov, O. Lalakulich, A.B. Larionov, T. Leitner, J. Weil, and U. Mosel, Transport-theoretical description of nuclear reactions, Phys. Rep. **512**, 1 (2012).
[9] T. Golan, C. Juszczak, and J. T. Sobczyk, Final state interactions effects in neutrino-nucleus interactions, Phys. Rev. C **86**, 015505 (2012).
[10] D. Drakoulakos *et al.* (MINERvA Collaboration), Proposal to perform a high-statistics neutrino scattering experiment using a fine-grained detector in the NuMI beam, arXiv:hep-ex/0405002.
[11] A. A. Aguilar-Arevalo *et al.* (MiniBooNE Collaboration), First measurement of the muon neutrino charged current quasielastic double differential cross section, Phys. Rev. D **81**, 092005 (2010).
[12] A. A. Aguilar-Arevalo *et al.* (MiniBooNE Collaboration), Measurement of neutrino-induced charged-current charged pion production cross sections on mineral oil at $E_\nu \sim 1$ GeV, Phys. Rev. D **83**, 052007 (2011).
[13] A. A. Aguilar-Arevalo *et al.* (MiniBooNE Collaboration), Measurement of the neutrino neutral-current elastic differential cross section on mineral oil at $E_\nu \sim 1$ GeV, Phys. Rev. D **82**, 092005 (2010).
[14] K. Abe *et al.* (T2K Collaboration), Measurements of neutrino oscillation in appearance and disappearance channels by the T2K experiment with 6.6×10^{20} protons on target, Phys. Rev. D **91**, 072010 (2015).
[15] C. Anderson *et al.* (ArgoNeuT Collaboration), First Measurements of Inclusive Muon Neutrino Charged Current

Differential Cross Sections on Argon, Phys. Rev. Lett. **108**, 161802 (2012).

[16] P. A. Rodrigues *et al.* (MINERvA Collaboration), Identification of nuclear effects in neutrino-carbon interactions at low three-momentum transfer, Phys. Rev. Lett. **116**, 071802 (2016).

[17] G. D. Megias, J. E. Amaro, M. B. Barbaro, J. A. Caballero, and T. W. Donnelly, Inclusive electron scattering within the SuSAv2-MEC approach, arXiv:1603.08396 [Phys. Rev. D (to be published)].

[18] A. Lovato, S. Gandolfi, R. Butler, J. Carlson, E. Lusk, S. C. Pieper, and R. Schiavilla, Charge Form Factor and Sum Rules of Electromagnetic Response Functions in ^{12}C, Phys. Rev. Lett. **111**, 092501 (2013).

[19] S. Bacca and S. Pastore, Electromagnetic reactions on light nuclei, J. Phys. G **41**, 123002 (2014).

[20] J. Carlson, S. Gandolfi, F. Pederiva, S. C. Pieper, R. Schiavilla, K. E. Schmidt, and R. B. Wiringa, Quantum Monte Carlo methods for nuclear physics, Rev. Mod. Phys. **87**, 1067 (2015).

[21] G. Lee, J. R. Arrington, and R. J. Hill (to be published).

[22] For a review see K. A. Olive *et al.* (Particle Data Group Collaboration), Review of particle physics, Chin. Phys. C **38**, 090001 (2014).

[23] V. Lyubushkin *et al.* (NOMAD Collaboration), A Study of quasi-elastic muon neutrino and antineutrino scattering in the NOMAD experiment, Eur. Phys. J. C **63**, 355 (2009).

[24] J. Brunner *et al.* (SKAT Collaboration), Quasielastic nucleon and hyperon production by neutrinos and antineutrinos with energies below 30-GeV, Z. Phys. C **45**, 551 (1990).

[25] M. Pohl *et al.* (GARGAMELLE NEUTRINO PROPANE Collaboration), Experimental study of the reaction $Nn \to M^- P$, Lett. Nuovo Cimento Soc. Ital. Fis. **26**, 332 (1979).

[26] L. B. Auerbach *et al.* (LSND Collaboration), Measurements of charged current reactions of muon neutrinos on C-12, Phys. Rev. C **66**, 015501 (2002).

[27] S. V. Belikov *et al.*, Quasielastic neutrino and anti-neutrinos scattering: Total cross-sections, axial vector form-factor, Z. Phys. A **320**, 625 (1985).

[28] S. Bonetti, G. Carnesecchi, D. Cavalli, P. Negri, A. Pullia, M. Rollier, F. Romano, and R. Schira, Study of quasielastic reactions of neutrino and anti-neutrino in Gargamelle, Nuovo Cim. A **38**, 260 (1977).

[29] For a review see: V. Bernard, L. Elouadrhiri, and U. G. Meissner, Axial structure of the nucleon: Topical review, J. Phys. G **28**, R1 (2002).

[30] V. A. Andreev *et al.* (MuCap Collaboration), Measurement of Muon Capture on the Proton to 1% Precision and Determination of the Pseudoscalar Coupling g_P, Phys. Rev. Lett. **110**, 012504 (2013).

[31] B. Bhattacharya, R. J. Hill, and G. Paz, Model independent determination of the axial mass parameter in quasielastic neutrino-nucleon scattering, Phys. Rev. D **84**, 073006 (2011).

[32] R. J. Hill and G. Paz, Model independent extraction of the proton charge radius from electron scattering, Phys. Rev. D **82**, 113005 (2010).

[33] I. T. Lorenz and U. G. Meißner, Reduction of the proton radius discrepancy by 3σ, Phys. Lett. B **737**, 57 (2014).

[34] Z. Epstein, G. Paz, and J. Roy, Model independent extraction of the proton magnetic radius from electron scattering, Phys. Rev. D **90**, 074027 (2014).

[35] G. Lee, J. R. Arrington, and R. J. Hill, Extraction of the proton radius from electron-proton scattering data, Phys. Rev. D **92**, 013013 (2015).

[36] B. Bhattacharya, G. Paz, and A. J. Tropiano, Model-independent determination of the axial mass parameter in quasielastic antineutrino-nucleon scattering, Phys. Rev. D **92**, 113011 (2015).

[37] For a review and further references see: R. J. Hill, in Proceedings of 4th Flavor Physics and *CP* Violation Conference (FPCP 2006), Vancouver, British Columbia, Canada, 2006, arXiv:hep-ph/0606023, p. 27.

[38] C. Bourrely, B. Machet, and E. de Rafael, Semileptonic decays of pseudoscalar particles ($M \to M' + \ell + \nu_\ell$) and short distance behavior of quantum chromodynamics, Nucl. Phys. **B189**, 157 (1981).

[39] C. G. Boyd, B. Grinstein, and R. F. Lebed, Constraints on Form Factors for Exclusive Semileptonic Heavy to Light Meson Decays, Phys. Rev. Lett. **74**, 4603 (1995).

[40] C. G. Boyd, B. Grinstein, and R. F. Lebed, Model-independent determinations of $B \to Dl\nu, D^* l\nu$ form-factors, Nucl. Phys. **B461**, 493 (1996).

[41] L. Lellouch, Lattice-constrained unitarity bounds for $\bar{B}0 \to \pi + \ell - \bar{\nu}_\ell$ decays, Nucl. Phys. **B479**, 353 (1996).

[42] I. Caprini, L. Lellouch, and M. Neubert, Dispersive bounds on the shape of $B \to D^* l\nu$ form factors, Nucl. Phys. **B530**, 153 (1998).

[43] C. M. Arnesen, B. Grinstein, I. Z. Rothstein, and I. W. Stewart, Precision Model Independent Determination of $|V_{ub}|$ from $B \to \pi l\nu$, Phys. Rev. Lett. **95**, 071802 (2005).

[44] T. Becher and R. J. Hill, Comment on form factor shape and extraction of $|V_{ub}|$ from $B \to \pi l\nu$, Phys. Lett. B **633**, 61 (2006).

[45] R. J. Hill, Constraints on the form factors for $K \to \pi l\nu$ and implications for $|V_{\mathrm{us}}|$, Phys. Rev. D **74**, 096006 (2006).

[46] C. Bourrely, L. Lellouch, and I. Caprini, Model-independent description of $B \to \pi l\nu$ decays and a determination of $|V_{ub}|$, Phys. Rev. D **79**, 013008 (2009).

[47] A. Bharucha, T. Feldmann, and M. Wick, Theoretical and phenomenological constraints on form factors for radiative and semi-leptonic B-meson decays, J. High Energy Phys. 09 (2010) 090.

[48] Y. Amhis *et al.* (Heavy Flavor Averaging Group (HFAG) Collaboration), Averages of *b*-hadron, *c*-hadron, and τ-lepton properties as of summer 2014, arXiv:1412.7515.

[49] C. Bouchard, G. P. Lepage, C. Monahan, H. Na, and J. Shigemitsu (HPQCD Collaboration), Rare decay $B \to K\ell^+\ell^-$ form factors from lattice QCD, Phys. Rev. D **88**, 054509 (2013); Publisher's Note, Phys. Rev. D **88**, 079901 (2013).

[50] J. A. Bailey *et al.*, $B \to Kl^+l^-$ decay form factors from three-flavor lattice QCD, Phys. Rev. D **93**, 025026 (2016).

[51] R. R. Horgan, Z. Liu, S. Meinel, and M. Wingate, Lattice QCD calculation of form factors describing the rare decays $B \to K^*\ell^+\ell^-$ and $B_s \to \phi\ell^+\ell^-$, Phys. Rev. D **89**, 094501 (2014).

[52] J. A. Bailey *et al.* (Fermilab Lattice and MILC Collaborations), $|V_{ub}|$ from $B \to \pi \ell \nu$ decays and $(2+1)$-flavor lattice QCD, Phys. Rev. D **92**, 014024 (2015).

[53] W. Detmold, C. Lehner, and S. Meinel, $\Lambda_b \to p\ell^- \bar{\nu}_\ell$ and $\Lambda_b \to \Lambda_c \ell^- \bar{\nu}_\ell$ form factors from lattice QCD with relativistic heavy quarks, Phys. Rev. D **92**, 034503 (2015).

[54] K. S. Kuzmin, V. Lyubushkin, and V. Naumov, Quasielastic axial-vector mass from experiments on neutrino-nucleus scattering, Eur. Phys. J. C **54**, 517 (2008).

[55] A. Bodek, S. Avvakumov, R. Bradford, and H. S. Budd, Vector and axial nucleon form factors: A duality constrained parameterization, Eur. Phys. J. C **53**, 349 (2008).

[56] G. A. Fiorentini *et al.* (MINERvA Collaboration), Measurement of Muon Neutrino Quasielastic Scattering on a Hydrocarbon Target at $E_\nu \sim 3.5$ GeV, Phys. Rev. Lett. **111**, 022502 (2013).

[57] W. A. Mann, U. Mehtani, B. Musgrave, Y. Oren, P. A. Schreiner, R. Singer, H. Yuta, R. Ammar *et al.*, Study of the Reaction $\nu + n \to \mu^- + p$, Phys. Rev. Lett. **31**, 844 (1973).

[58] S. J. Barish, J. Campbell, G. Charlton, Y. Cho, M. Derrick, R. Engelmann, L. G. Hyman, D. Jankowski *et al.*, Study of neutrino interactions in hydrogen and deuterium. Description of the experiment and study of the reaction $\nu + d \to \mu^- + p + p_s$, Phys. Rev. D **16**, 3103 (1977).

[59] K. L. Miller, S. J. Barish, A. Engler, R. W. Kraemer, B. J. Stacey, M. Derrick, E. Fernandez, L. Hyman *et al.*, Study of the reaction $\nu_\mu d \to \mu^- p p_s$, Phys. Rev. D **26**, 537 (1982).

[60] N. J. Baker, A. M. Cnops, P. L. Connolly, S. A. Kahn, H. G. Kirk, M. J. Murtagh, R. B. Palmer, N. P. Samios, and M. Tanaka, Quasielastic neutrino scattering: A measurement of the weak nucleon axial vector form factor, Phys. Rev. D **23**, 2499 (1981).

[61] T. Kitagaki, S. Tanaka, H. Yuta, K. Abe, K. Hasegawa, A. Yamaguchi, K. Tamai, T. Hayashino *et al.*, High-energy quasielastic $\nu_\mu n \to \mu^- p$ scattering in deuterium, Phys. Rev. D **28**, 436 (1983).

[62] T. Kitagaki *et al.*, Study of $\nu d \to \mu^- p p_s$ and $\nu d \to \mu^- \Delta^{++}(1232) n_s$ using the BNL 7-foot deuterium filled bubble chamber, Phys. Rev. D **42**, 1331 (1990).

[63] M. G. Olsson, E. T. Osypowski, and E. H. Monsay, Electroproduction of low hadronic masses, Phys. Rev. D **17**, 2938 (1978). See in particular Eq. (5).

[64] R. Bradford, A. Bodek, H. S. Budd, and J. Arrington, A new parameterization of the nucleon elastic form factors, Nucl. Phys. B, Proc. Suppl. **159**, 127 (2006).

[65] S. K. Singh, The effect of final state interactions and deuteron binding in neutrino $\nu d \to \mu^- p p$, Nucl. Phys. **B36**, 419 (1972).

[66] H. S. Budd, A. Bodek and J. Arrington, Modeling quasielastic form factors for electron and neutrino scattering, arXiv:hep-ex/0308005.

[67] A. Bodek, S. Avvakumov, R. Bradford, and H. S. Budd, Vector and axial nucleon form factors: A duality constrained parameterization, Eur. Phys. J. C **53**, 349 (2008).

[68] R. Pohl *et al.*, The size of the proton, Nature (London) **466**, 213 (2010).

[69] J. C. Bernauer *et al.* (A1 Collaboration), Electric and magnetic form factors of the proton, Phys. Rev. C **90**, 015206 (2014).

[70] G. Shen, L. E. Marcucci, J. Carlson, S. Gandolfi, and R. Schiavilla, Inclusive neutrino scattering off deuteron from threshold to GeV energies, Phys. Rev. C **86**, 035503 (2012).

[71] C. H. Llewellyn Smith, Neutrino reactions at accelerator energies, Phys. Rep. **3**, 261 (1972).

[72] See Supplemental Material at http://link.aps.org/supplemental/10.1103/PhysRevD.93.113015 for the digitized dN/dQ^2 and dN/dE files from the ANL, BNL, and FNAL experiments as well as smeared dN/dE distributions.

[73] S. J. Barish *et al.*, Study of neutrino interactions in hydrogen and deuterium: Inelastic charged current reactions, Phys. Rev. D **19**, 2521 (1979).

[74] A. Bodek, H. S. Budd, and J. Arrington, Modeling neutrino quasielastic cross-sections on nucleons and nuclei, AIP Conf. Proc. **698**, 148 (2004).

[75] H. S. Budd, A. Bodek, and J. Arrington, Vector and axial form-factors applied to neutrino quasielastic scattering, Nucl. Phys. B, Proc. Suppl. **139**, 90 (2005).

[76] G. P. Lepage and S. J. Brodsky, Exclusive processes in perturbative quantum chromodynamics, Phys. Rev. D **22**, 2157 (1980).

[77] K. L. Miller, Ph. D. thesis, Carnegie Mellon University, 1981, Report No. UMI-92-09392.

[78] M. Martini, M. Ericson, G. Chanfray, and J. Marteau, A unified approach for nucleon knock-out, coherent and incoherent pion production in neutrino interactions with nuclei, Phys. Rev. C **80**, 065501 (2009).

[79] R. Gran, J. Nieves, F. Sanchez, and M. J. Vicente Vacas, Neutrino-nucleus quasi-elastic and 2p2h interactions up to 10 GeV, Phys. Rev. D **88**, 113007 (2013).

[80] S. K. Singh and H. Arenhovel, Pion exchange current effects in $\upsilon_\mu + d \to \mu^- + p + p$, Z. Phys. A **324**, 347 (1986).

[81] O. Moreno, T. W. Donnelly, J. W. Van Orden, and W. P. Ford, Coincidence charged-current neutrino-induced deuteron disintegration, Phys. Rev. D **92**, 053006 (2015).

[82] M. Betancourt, Muon Neutrino CCQE at MINERvA, Nuint 2015 conference proceedings (to be published).

[83] J. E. Amaro and E. Ruiz Arriola, Axial-vector dominance predictions in quasielastic neutrino-nucleus scattering, Phys. Rev. D **93**, 053002 (2016).

[84] F. Simkovic, A. Faessler, V. Rodin, P. Vogel, and J. Engel, Anatomy of nuclear matrix elements for neutrinoless double-beta decay, Phys. Rev. C **77**, 045503 (2008).

[85] J. D. Holt and J. Engel, Effective double-β-decay operator for ^{76}Ge and ^{82}Se, Phys. Rev. C **87**, 064315 (2013).

[86] For a review and further references, see A. Bazavov *et al.* (MILC Collaboration), Nonperturbative QCD simulations with $2+1$ flavors of improved staggered quarks, Rev. Mod. Phys. **82**, 1349 (2010).

[87] S. Dinter, C. Alexandrou, M. Constantinou, V. Drach, K. Jansen, and D. B. Renner, Precision study of excited state effects in nucleon matrix elements, Phys. Lett. B **704**, 89 (2011).

[88] A. Bazavov *et al.*, Lattice QCD ensembles with four flavors of highly improved staggered quarks, Phys. Rev. D **87**, 054505 (2013).

[89] T. Bhattacharya, S. D. Cohen, R. Gupta, A. Joseph, H.-W. Lin, and B. Yoon, Nucleon charges and electromagnetic form factors from $2+1+1$-flavor lattice QCD, Phys. Rev. D **89**, 094502 (2014).

[90] J. R. Green, M. Engelhardt, S. Krieg, J. W. Negele, A. V. Pochinsky, and S. N. Syritsyn, Nucleon structure from lattice QCD using a nearly physical pion mass, Phys. Lett. B **734**, 290 (2014).

[91] A. Bazavov *et al.* (Fermilab Lattice and MILC Collaborations), The nucleon axial-vector form factor at the physical point with HISQ ensembles (unpublished).